



Corrosion of lithium metal anodes during calendar ageing and its microscopic origins

David T. Boyle^{ID 1,5}, William Huang^{ID 2,5}, Hansen Wang^{ID 2}, Yuzhang Li², Hao Chen^{ID 2}, Zhiao Yu^{ID 1,3}, Wenbo Zhang², Zhenan Bao^{ID 3} and Yi Cui^{ID 2,4}✉

Rechargeable lithium (Li) metal batteries must have long cycle life and calendar life (retention of capacity during storage at open circuit). Particular emphasis has been placed on prolonging the cycle life of Li metal anodes, but calendar ageing is less understood. Here, we show that Li metal loses at least 2–3% of its capacity after only 24 hours of ageing, regardless of the electrolyte chemistry. These losses of capacity during calendar ageing also shorten the cycle life of Li metal batteries. Cryogenic transmission electron microscopy shows that chemical corrosion of Li and the continuous growth of the solid electrolyte interphase—a passivation film on Li—cause the loss of capacity. Electrolytes with long cycle life do not necessarily form a solid electrolyte interphase with more resistance to chemical corrosion, so functional electrolytes must simultaneously minimize the rate of solid electrolyte interphase growth and the surface area of electrodeposited Li metal.

Rechargeable Li metal batteries (LMBs) could meet demand for higher energy density batteries, as the metallic Li anode has an excellent capacity and standard redox potential (3,860 mAh g⁻¹, -3.04 V versus the standard hydrogen electrode)^{1–3}. Widespread adoption of LMBs requires that Li anodes retain capacity after many cycles (that is, have a long cycle life) and periods of storage at open circuit (that is, have a long calendar life). Recently, nanoscopic characterization of Li with techniques such as cryogenic transmission electron microscopy (cryo-TEM)^{4–8} and several engineering strategies have improved the cycle life of Li metal anodes^{9–13}. However, tests of Li metal anodes often neglect calendar ageing^{14–16}, and even though the electrolyte strongly influences battery performance, characterization is usually limited to a small set of electrolyte chemistries^{5–8}. Previous work showed that incomplete passivation and high areal exposure of the current collector to the electrolyte can cause galvanic corrosion of Li during calendar ageing^{17,18}. Much less is known about how chemical corrosion (that is, solid electrolyte interphase (SEI) growth at the Li metal surface) and the electrolyte chemistry affect the calendar ageing of Li metal anodes.

Although the effects of calendar ageing on LMBs are unclear, they are well known for Li ion batteries (LIBs) with graphite intercalation anodes^{19–21}. In LIBs, reduction of the electrolyte at the anode surface and growth of the SEI cause most capacity losses during calendar ageing^{19,20}. Losses are accelerated when the graphite anode is fully charged (lithiated) to a potential of about 10 mV versus Li/Li⁺, thereby increasing the thermodynamic driving force for electrolyte reduction²⁰. To minimize these losses, a strongly passivating SEI is carefully formed on graphite during initial cycling²², and LIBs are generally stored at partially charged states²⁰. In LMBs, however, fresh surfaces of Li metal are exposed during each electrodeposition, so the SEI must be re-formed during each charging step⁶, and the potential of Li metal is always 0 V versus Li/Li⁺ at open circuit. These two key features make the calendar ageing of LMBs uniquely important to understand.

In this work, we reveal the effects of calendar ageing on the rechargeability of Li metal anodes and LMBs. Coulometric methods

quantify the irreversible loss of capacity during calendar ageing of Li in a variety of electrolyte chemistries. Combining these results with cryo-scanning TEM (cryo-STEM) mapping of Li aged in several electrolytes shows that the growth of SEI is the general cause of the capacity loss. The distinct SEI growth rate and surface areas of Li in each electrolyte determine the magnitude of the loss. This combination of electrochemical analysis, nanoscale materials characterization and electrolyte variety provides a technical pathway for further studies to understand calendar ageing and SEI growth in LMBs.

Capacity loss during ageing

Coulombic efficiency (CE) measurements with a Li||Cu half-cell are often used to quantify the rechargeability of Li metal in a particular electrolyte¹⁴. The CE quantifies the ratio of Li output during discharge (stripping) to Li input during charge (plating). This method conveniently tests the reversibility of Li electrodeposition and dissolution, but calendar ageing steps are generally excluded (Supplementary Fig. 1a). Here, we age the cells for 24 hours at open circuit after the plating step of the second cycle (Supplementary Fig. 1b). The difference between the CE of Li with and without calendar ageing quantifies the extra loss of capacity:

$$\Delta\text{CE} = \text{CE}_{\text{2nd cycle}}^{\text{with ageing}} - \text{CE}_{\text{2nd cycle}}^{\text{no ageing}}. \quad (1)$$

Comparisons of ΔCE with Li||Cu cells in a variety of electrolytes and operating conditions provide a simple platform to understand the underlying causes of capacity loss in LMBs.

First, we measured ΔCE in a variety of electrolyte chemistries from the literature, as the average CE of the first 20 cycles without ageing depends on the electrolyte chemistry (Fig. 1a and Supplementary Fig. 2). We chose a sample of electrolytes that is representative of commercially available carbonate electrolytes and recently developed high-CE electrolytes^{11,23,24} (details in Fig. 1 caption). The chosen high-CE electrolytes typify several strategies, such as using two salts, additives, high salt concentrations

¹Department of Chemistry, Stanford University, Stanford, CA, USA. ²Department of Materials Science and Engineering, Stanford University, Stanford, CA, USA. ³Department of Chemical Engineering, Stanford University, Stanford, CA, USA. ⁴Stanford Institute for Materials and Energy Sciences, SLAC National Accelerator Laboratory, Menlo Park, CA, USA. ⁵These authors contributed equally: David T. Boyle, William Huang. ✉e-mail: yicui@stanford.edu

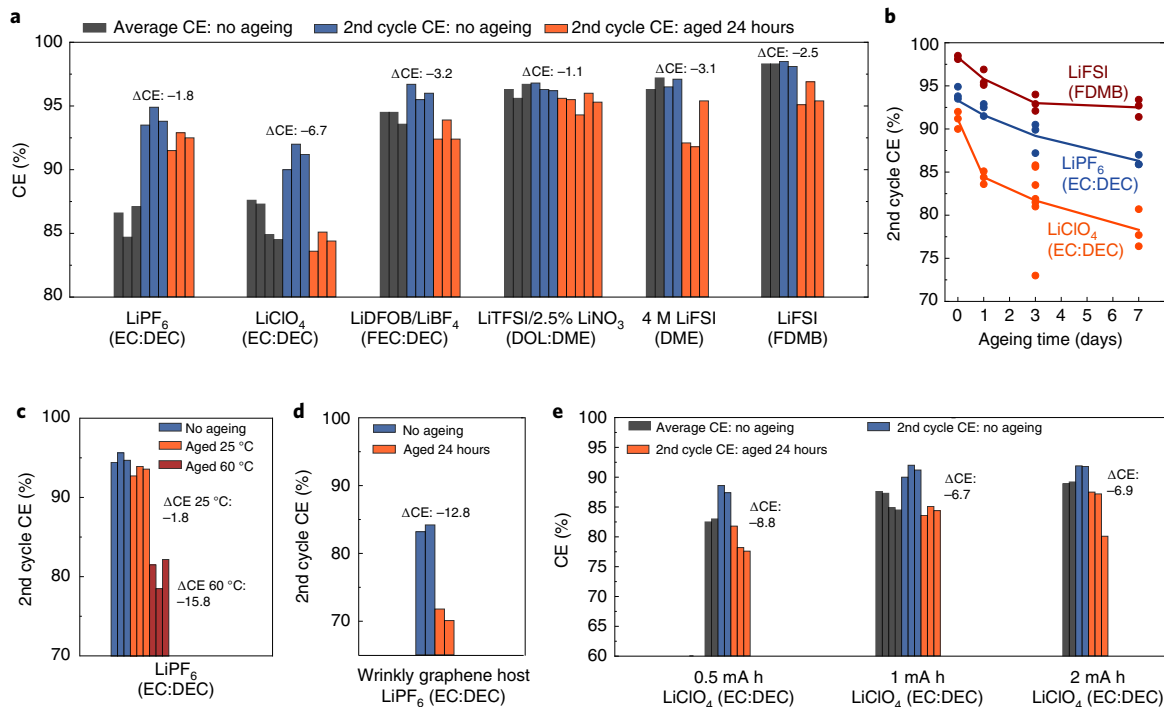


Fig. 1 | Effect of resting intervals on the CE of lithium metal anodes. **a**, The CE of lithium metal in a variety of electrolytes. These electrolytes include 1 M LiPF₆ in EC:DEC, 1 M LiClO₄ in EC:DEC, 0.6 M LiDFOB and 0.6 M LiBF₄ in FEC:DEC, 1 M LiTFSI with 2.5% LiNO₃ in DOL:DME, 4 M LiFSI in DME and 1 M LiFSI in FDMB. Each bar represents a single data point or cell. **b**, The second cycle CE of Li as a function of calendar ageing time. Each dot represents a single data point or cell. **c,d**, The effect of temperature (**c**) and Li hosts (**d**) on ΔCE after 24 hours of calendar ageing. **e**, The effect of the capacity of Li on ΔCE.

and fluorinated solvent. Our modified CE protocol shows that the CE of Li decreases by 2–3% after 24 hours of calendar ageing in most electrolytes and up to 6.7% in LiClO₄ (in ethylene carbonate:diethylcarbonate (EC:DEC); Fig. 1a and Supplementary Fig. 3). Interestingly, ΔCE is relatively consistent across electrolytes, with average CE varying between 85–99% (Fig. 1a). For example, the average CE of Li is 85.5% in LiPF₆ (EC:DEC) and 98.8% in LiFSI (fluorinated 1,4-dimethoxybutane (FDMB)), but these electrolytes have a ΔCE of −1.8% and −2.5%, respectively. Capacity losses with Li metal anodes are generally caused by either SEI growth or the electrical disconnection of Li filaments during dissolution (that is, ‘dead Li’)⁴. This finding suggests that the growth of SEI during calendar ageing may cause ΔCE, because electrolytes with a CE > 95% are known to have minimal amounts of dead Li^{4,6,18}. It is generally thought that high-CE electrolytes have strongly passivating SEI, so the similar magnitude of ΔCE in both low- and high-CE electrolytes is somewhat surprising^{11,23–25}. To explain the magnitude of ΔCE in each electrolyte, both the surface area of Li and the rate of corrosion must be considered. These two factors are discussed later in the text after we demonstrate that SEI growth causes ΔCE.

Extended ageing times increase the magnitude of ΔCE, but at decreasing rates (Fig. 1b). During the first 72 hours of calendar ageing, the CE of Li decreases by an average of 1.8% per day, 1.3% per day and 3.1% per day in LiFSI (FDMB), LiPF₆ (EC:DEC) and LiClO₄ (EC:DEC), respectively. After the first 72 hours, the rate of capacity loss slows to 0.1% per day, 0.7% per day and 0.9% per day, respectively. The smoothly decreasing rate of capacity loss is consistent with SEI growth, which is self-passivating²⁶. The continuity of the data in Fig. 1b also suggests that large amounts of dead Li are not formed during ageing, because this would likely cause sharp discontinuities in the data.

Operational conditions like temperature more strongly affect ΔCE (Fig. 1c). If the cell is aged at 60 °C instead of 25 °C, then ΔCE

increases by an order of magnitude (−1.8% to −16.6% in LiPF₆ (EC:DEC)). This result is consistent with observations of aged LIBs, where high temperatures accelerate the reduction of electrolyte at the anode and cause SEI growth²⁰. Although high temperatures are reported to improve the cycle life of LMBs in some electrolytes^{11,27,28}, LMBs should be stored at low temperatures.

Nanostructured Li hosts improve the CE of Li by minimizing dead Li^{4,6} and the impedance of the anode^{2,29}, but this comes at the cost of higher electrochemically active surface area. Comparing ΔCE with planar Cu foil to a nanostructured wrinkly graphene host²⁹ of the same geometric area shows that ΔCE increases from −1.8% to −12.8%, respectively (Fig. 1d). This scaling of ΔCE with surface area provides further evidence that SEI growth causes ΔCE. Such a large initial capacity loss with nanostructured hosts highlights the importance of using prelithiation⁹, which provides excess Li and minimizes surface area, or the interfacial stabilization¹³ of host materials.

Reduction of the electrolyte to form SEI can occur through two distinct pathways: reduction at the Li surface via chemical corrosion^{17,26} and reduction at the surface of the Cu current collector through galvanic corrosion^{17,18}. The contribution of each pathway to capacity loss depends on the design of the cell or parameters of Li deposition. Chemical corrosion scales with the surface area and capacity of deposited Li. Galvanic corrosion scales with the surface area of Cu, which decreases—relative to the surface area of Li—with higher capacities of deposited Li^{18,30}. Recent work proposed that galvanic corrosion can cause 80% of ΔCE, but the area of Cu was much larger than Li. Only 50 μA h cm^{−2} of Li was deposited¹⁸. To estimate the contribution of each pathway for more practical capacities, we measured ΔCE for 0.5, 1 and 2 mA h cm^{−2} of Li (Fig. 1e and Supplementary Fig. 4). The consistent ΔCE (%) suggests that the absolute loss of Li scales with the capacity, meaning chemical corrosion plays a larger role than galvanic corrosion for higher

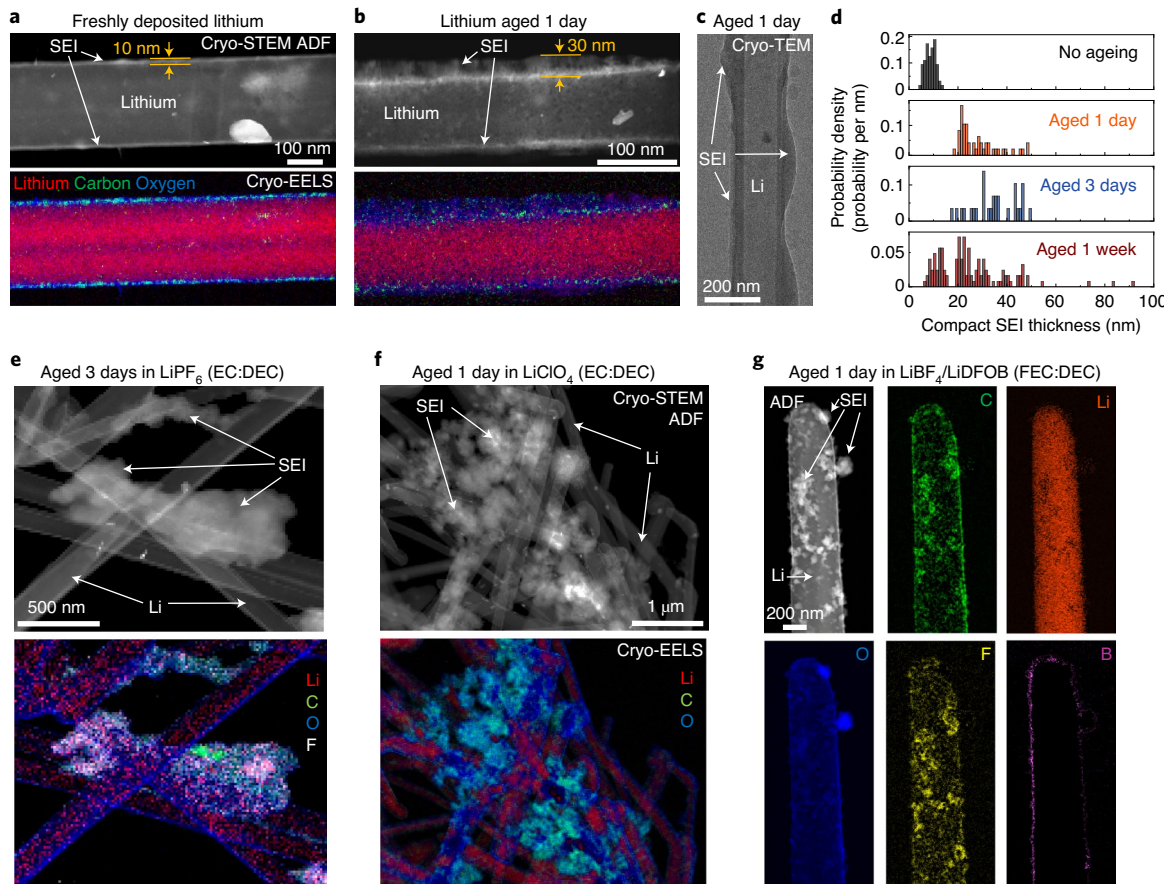


Fig. 2 | Cryo-(S)TEM mapping of SEI growth on Li metal during calendar ageing in both low- and high-performance electrolytes. **a,b**, Representative cryo-STEM ADF image and EELS map of freshly deposited Li (**a**) and Li aged for 24 hours in LiPF_6 (EC:DEC) (**b**). **c**, Representative bright-field TEM image of a Li filament after calendar ageing in LiPF_6 (EC:DEC). **d**, Histogram of the time-dependent thickness of the compact SEI. **e–g**, Cryo-STEM ADF images and EELS maps of a Li anode aged in LiPF_6 (EC:DEC) (**e**), LiClO_4 (EC:DEC) (**f**) and $\text{LiBF}_4/\text{LiDFOB}$ (FEC:DEC) (**g**) with representative examples of extended SEIs.

areal capacities of Li. This analysis only provides a crude estimate. Exact quantification of the contribution of each distinct pathway using simple electroanalysis is difficult in practice. Regardless, both pathways cause SEI growth. Strongly passivating coatings like LiF may minimize chemical corrosion like they do with galvanic corrosion¹⁸, but an explicit study of its role on ΔCE requires a quantitative comparison of the surface area of Li that is beneath the coating and exposed to the electrolyte. Any strategy to improve Li metal anodes should emphasize the formation of a more passivating SEI.

Chemical corrosion and SEI growth

Cryo-STEM electron energy loss spectroscopy (EELS) mapping of Li anodes before and after calendar ageing confirms that SEI growth is the primary cause of ΔCE . This technique stabilizes Li and its SEI, which are sensitive to air and the electron beam, and simultaneously provides nanoscopic structural and chemical information to track the growth of SEI during ageing^{5,7,31}. Figure 2a shows a representative cryo-STEM image of Li with a conformal and thin 10 nm SEI after being freshly deposited in LiPF_6 (EC:DEC)—consistent with previous studies of this system^{5–8}. The annular dark field (ADF) STEM image shows a low intensity core from the low atomic number of Li ($Z=3$). The brighter intensity shell is attributed to the SEI and its C- and O-rich composition (Fig. 2a), which is consistent with previous characterization of the SEI formed in EC electrolytes^{4,5,7,32}. This form of SEI is often called the compact SEI²⁶, as it exists as a thin film and is directly interfaced with Li. After Li anodes are aged in the electrolyte for 24 hours, the thickness of the compact SEI

noticeably increases. A lower density layer grows above the initially formed SEI (Fig. 2b). We also occasionally observe local pitting of Li filaments (Supplementary Fig. 5), which could form dead Li during calendar ageing, but this is rare compared to the growth of SEI. Extra dead Li is not likely the main cause of ΔCE , as it is rarely seen with cryo-STEM, the ΔCE versus time data are continuous (Fig. 1b) and ΔCE is independent of the stripping current density (Supplementary Fig. 6). We note that a previous study of calendar aged Li powder electrodes showed that dead Li was a major source of capacity loss¹⁷. In that report, high exposure of Cu to the electrolyte, which causes substantial galvanic corrosion at the $\text{Li}||\text{Cu}$ interface, and a looser electrical connection of the Li powder network explain the larger role of dead Li. In our work, the exposure of Cu is much less than Li, and the Li deposits have a much stronger electrical connection. Nevertheless, dead Li should remain minimized.

Although models of SEI growth often describe the SEI as a conformal film^{26,33}, the growth of the compact SEI is highly heterogeneous over the nanoscale (Fig. 2c). We quantified the time-dependent thickness and heterogeneity of the compact SEI in LiPF_6 (EC:DEC) with high resolution cryo-TEM (Fig. 2d and Supplementary Fig. 7). The compact SEI on freshly deposited Li has an average thickness of 8.8 nm, and all measured thicknesses are within 7–15 nm. After 24 and 72 hours of calendar ageing, the average thickness increases to 28.4 and 34.9 nm, respectively. The spread of measured thicknesses after 24 and 72 hours of ageing also increases to 20–40 nm. These trends are not limited to only LiPF_6 (EC:DEC) electrolyte. Li aged 24 hours in LiClO_4 (EC:DEC) and $\text{LiBF}_4/\text{LiDFOB}$ (fluoroethylene

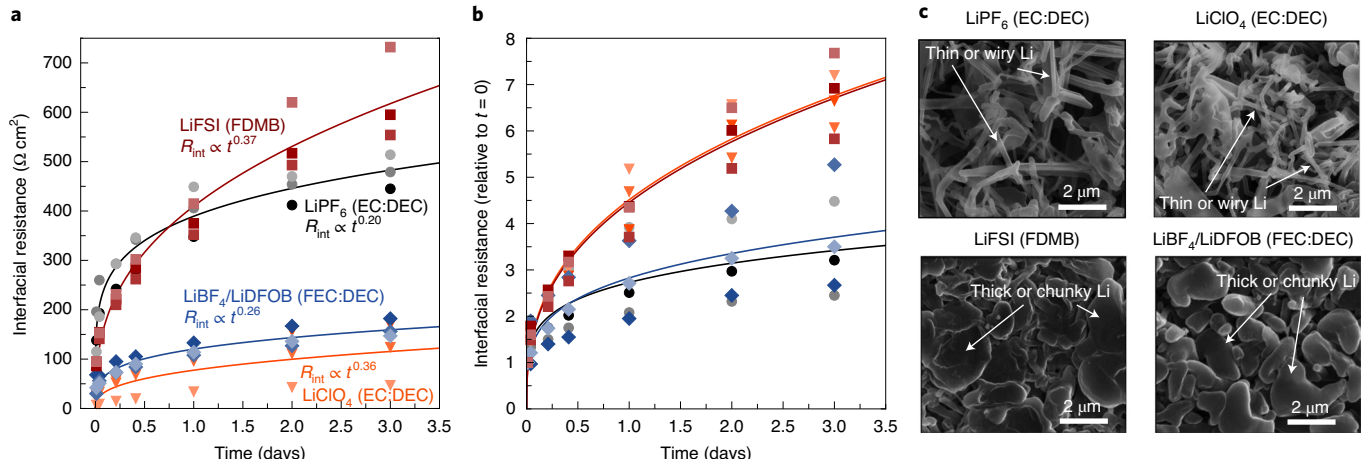


Fig. 3 | Time-dependent interfacial resistance and microstructure of electrodeposited Li metal in select electrolytes. **a**, $R_{int}(t)$ and corresponding non-linear least squares fit to a power law. Shades of each colour represent an independent Li||Li cell with the same electrolyte. **b**, $R_{int}(t)$ plotted relative to $R_{int}(t=0)$. The shapes and colours correspond to the same electrolytes labelled in **a**. **c**, Scanning electron microscopy images of freshly electrodeposited Li on Cu.

carbonate (FEC):DEC) had average SEI thicknesses increase from 7.6 to 20.9 and 8.9 to 14.8 nm, respectively (Supplementary Fig. 8). The compact SEI on Li aged in LiPF₆ (EC:DEC) for 168 hours has a slightly smaller average thickness of 25.1 nm (potentially caused by experimental error in TEM statistics or SEI dissolution), but the spread of thicknesses increased to 7–92 nm. These results highlight the importance of using cryo-(S)TEM to characterize the thickness and distribution of phases of the SEI. X-ray photoelectron spectroscopy (XPS) of Li foils also suggests the SEI grows during calendar ageing (Supplementary Fig. 9), but XPS¹⁰ and other tools like secondary ion mass spectrometry^{34,35} typically require depth profiling methods and may not capture nanoscopic heterogeneities.

In addition to the growth of the compact SEI, we observe an extended and irregular form of SEI on Li aged for 24 hours and longer in several electrolytes (Fig. 2e–g and Supplementary Figs. 10–12). This form of SEI generally spans length scales (hundreds of nanometres) greater than the compact SEI (tens of nanometres) and is not necessarily in direct contact with Li. Compact and extended SEIs have been reported for carbon^{26,31} and Li electrodes⁵ in commercial carbonate electrolytes, where they are typically described as an inner (inorganic) layer and an outer (organic) layer. These cryo-(S)TEM data suggest that the growth of an extended SEI is general to all electrolyte chemistries, but the morphology and chemistry is unique to each electrolyte. Comparison of the extended SEI in each electrolyte can provide insight into its formation and role in ΔCE.

The extended SEI on Li aged in LiPF₆ (EC:DEC) appears as dense clumps, with a chemically unique, high fluorine content (Fig. 2e and Supplementary Fig. 11b). Selected area electron diffraction (Supplementary Fig. 13) and the EELS F K edge (Supplementary Fig. 14) suggest these clumps are rich in LiF, likely arising from the reduction of HF impurities^{36,37}. Precipitation of LiF outside of the compact SEI has been observed previously in carbonate electrolytes^{36,38}; here, we observe their temporal dependence and show that they form on long timescales during calendar ageing. The EELS C K edge of the compact and extended SEI both display strong CO₃ peaks^{39–41}, but the extended SEI has a much stronger C–H signal (Supplementary Fig. 15). This result suggests that the carbonaceous components of both SEI types contain carbonates, but the extended SEI is composed of more soluble, organic compounds such as carbonate-based polymers^{42,43}. Simply changing the salt to LiClO₄ results in much more abundant extended SEIs that appear as large, porous clumps of particles that span lengths up to

several micrometres (Fig. 2f). Larger amounts of extended SEI with LiClO₄ are consistent with the larger magnitude of ΔCE (−6.4% versus −1.8% with LiPF₆). The EELS C K edge of this extended SEI also shows a strong C–H signal compared to the compact SEI (Supplementary Fig. 16), but a Cl signal is absent in the EELS spectra (Supplementary Fig. 17). The strong passivity of LiF particles may cause the smaller magnitude of ΔCE in LiPF₆, relative to LiClO₄ (EC:DEC).

To confirm the generality of an extended SEI, we also investigated Li aged for 24 hours in LiBF₄/LiDFOB (FEC:DEC), which has an average CE of 94.2%. An extended SEI composed of particles less than 200 nm in length forms on the aged Li (Fig. 2g and Supplementary Fig. 12), whereas freshly deposited Li has only a compact SEI (Supplementary Fig. 18). Instead of clumping together, these particles decorate the surface of the Li. EELS spectra indicate that these particles are an organic material rich in C, O and F (Fig. 2g), consistent with previous characterization¹¹. Notably, only the compact SEI is rich in B. This chemical divergence suggests that the compact SEI is derived from the BF₄[−] and DFOB[−], and the extended SEI is mainly composed of more soluble reduction products of the FEC solvent.

Collectively, the cryo-STEM EELS mapping explicitly demonstrates that the growth of a compact and extended SEI is the primary cause of ΔCE. This finding provides a time-dependent picture of SEI growth and capacity loss in LMBs. At short times, the compact SEI grows via direct reduction of the electrolyte at the Li (or Cu) surface, where insoluble decomposition products (for example, Li₂O and Li₂CO₃) precipitate firstly and directly on the surface. In traditional models, further growth of the SEI proceeds through diffusion of the solvent to the anode–SEI interface or diffusion of electrons to the SEI–electrolyte interface³³. This pathway may explain the growth of the compact SEI, which does in fact thicken like a film, albeit nonuniformly. However, the extended SEI appears to precipitate as large clusters across the electrode, suggesting pathways that involve soluble decomposition products. For example, soluble radical species formed during the initial reduction reactions could propagate in the liquid phase until sufficiently insoluble products, such as carbonate-based polymers, precipitate onto the electrode^{31,42–44}. Similarly, soluble decomposition products (for example, lithium ethylene dicarbonate)⁵ could dissolve until they saturate the electrolyte and precipitate on the electrode. These precipitates will ultimately increase the interfacial impedance, which can cause extra losses of capacity. To minimize ΔCE, the solubility of electrolyte decomposition products should be minimized.

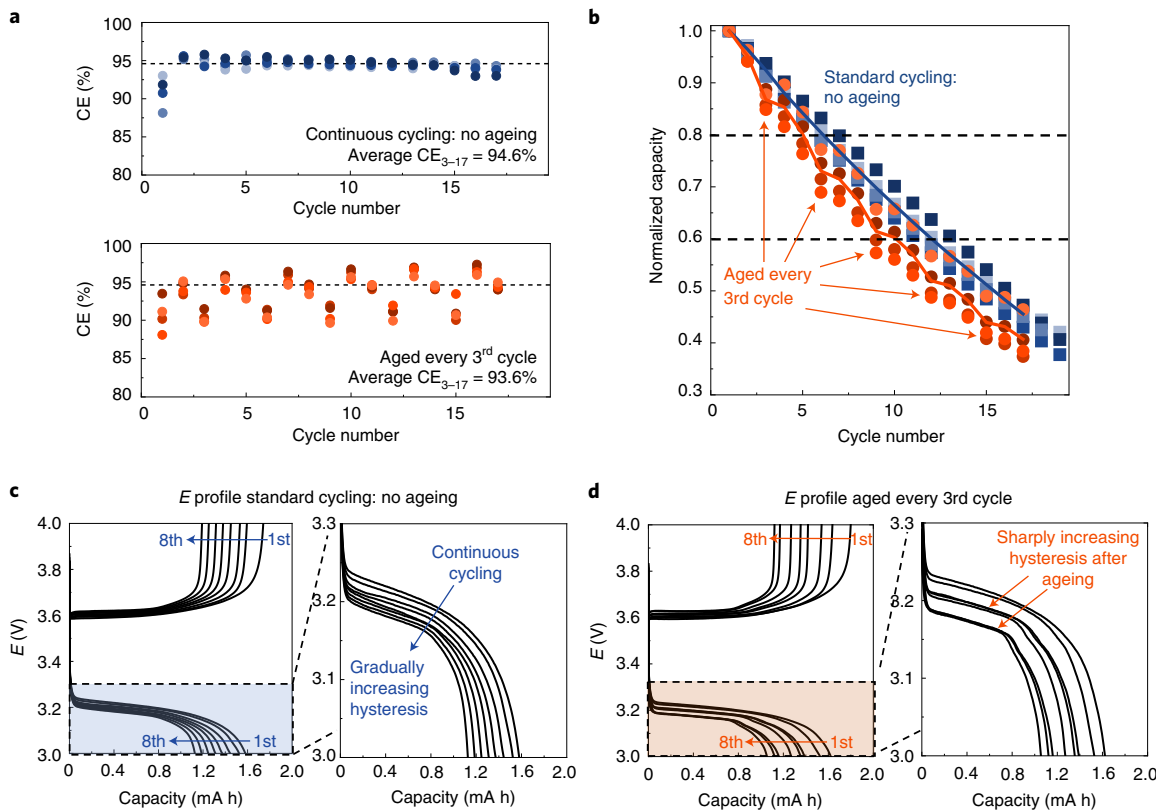


Fig. 4 | Effect of calendar ageing on the cycle life of anode-free full-cells. The full-cells use the LiBF₄/LiDFOB (FEC:DEC) electrolyte and a LFP cathode (2 mAh cm⁻² loading, cycling at C/2, 1 mA cm⁻²). a, CE of LFP anode-free free cells without calendar ageing (blues) and with ageing during every third cycle (oranges). Each shade of colour represents a particular full-cell and directly corresponds to the capacity data in b. Dashed lines are drawn at the average CE without ageing during cycles 3–17 (CE₃₋₁₇, 94.6%) to highlight deviations of the CE. b, Normalized discharge capacities without (blues) and with (oranges) calendar ageing during every third cycle. Each shade of colour represents a particular full-cell, and the averages of four cells are tracked with the solid lines. Arrows indicate the cycles with ageing intervals, and dashed lines indicate 80 and 60% capacity retention. c, Representative *E* profiles of the first eight cycles with a zoomed-in view of the discharge process for cells without ageing. d, Representative *E* profiles of the first eight cycles with calendar ageing during every third cycle with a zoomed-in view of the discharge process.

Coulometry and cryo-STEM show that growth of the SEI causes ΔCE, but neither explains why ΔCE is similar in electrolytes with CE ranging from 85–99%. Usually, Li is believed to be resistant to corrosion and SEI growth in high-CE electrolytes. Figure 1a suggests this expectation may not necessarily be true. To explain this surprising result, we measured the time-dependent interfacial resistance of Li ($R_{\text{int}}(t)$)—which is dominated by Li ion transport through the SEI^{45,46}—using electrochemical impedance spectroscopy (EIS; Fig. 3 and Supplementary Fig. 19). Quantifying $R_{\text{int}}(t)$ of Li||Li symmetric cells tracks the growth of SEI over a well-controlled surface area, making a comparison of different rates of SEI growth between electrolytes feasible.

Figure 3a shows that each electrolyte causes a distinct temporal evolution of $R_{\text{int}}(t)$, and hence, SEI growth. Fitting $R_{\text{int}}(t)$ to a power law (that is $R_{\text{int}} \propto at^x$), often used to empirically describe SEI growth^{26,47,48}, allows for a more quantitative comparison even though EIS averages out the nanoscopic heterogeneities of the SEI. The values of a and t^x are generally thought of as being proportional to the average resistivity and thickness of the SEI, respectively^{26,47,48}. Explicit comparisons of this model to microscopic phenomenon (for example, SEI thickness or SEI chemistry) have limitations, but it can still provide general insight. Early studies of SEI with EIS correctly predicted the compact and extended structure of SEI, despite several simple assumptions such as the SEI having a uniform dielectric constant^{49–51}. Our model is most useful for comparing the relative rates of SEI growth^{26,47,48}. The power law fits well to $R_{\text{int}}(t)$

(Fig. 3a and Supplementary Tables 1 and 2), and distinct scaling factors are calculated for each electrolyte (for example, $x=0.20$ for LiPF₆ (EC:DEC) and $x=0.37$ for LiFSI (FDMB); Fig. 3a). The scaling of $R_{\text{int}}(t)$ shows that the growth rate of the SEI (per surface area of Li) follows the order of LiClO₄ (EC:DEC) ≈ LiFSI (FDMB) > LiBF₄/LiDFOB (FEC:DEC) > LiPF₆ (EC:DEC). This trend becomes clearer when $R_{\text{int}}(t)$ is plotted relative to $R_{\text{int}}(t=0)$ for each electrolyte (Fig. 3b). After three days of calendar ageing, R_{int} increases by a factor of seven in LiClO₄ (EC:DEC) and LiFSI (FDMB). The R_{int} increases by a factor of only three to four in LiBF₄/LiDFOB (FEC:DEC) and LiPF₆ (EC:DEC). These data demonstrate that electrolytes with high CE may not necessarily have strong resistance to SEI growth during calendar ageing.

Comparison of the EIS data to the microstructure of deposited Li in the ΔCE measurements shows that an interplay between the rate of SEI growth and surface area of Li controls the value of ΔCE (that is, $\Delta\text{CE} \propto \text{rate}_{\text{SEI growth}} \times A_{\text{Li}}$). Li deposited in both LiClO₄ and LiPF₆ in EC:DEC has a thin or wiry microstructure (Fig. 3c). In LiClO₄ (EC:DEC), the high surface area and high rate of SEI growth result in the highest value of ΔCE, −6.4%. The lower rate of SEI growth in LiPF₆ in EC:DEC causes ΔCE to decrease to −1.8%. Li deposited in LiFSI (FDMB) and LiBF₄/LiDFOB (FEC:DEC) has a thick or chunky microstructure (Fig. 3c), which lowers its surface area and results in a high CE by limiting dead Li⁴. Despite the lower surface area in these electrolytes, the higher rates of SEI growth per area cause ΔCE to be similar in magnitude to that of LiPF₆ (EC:DEC). This finding

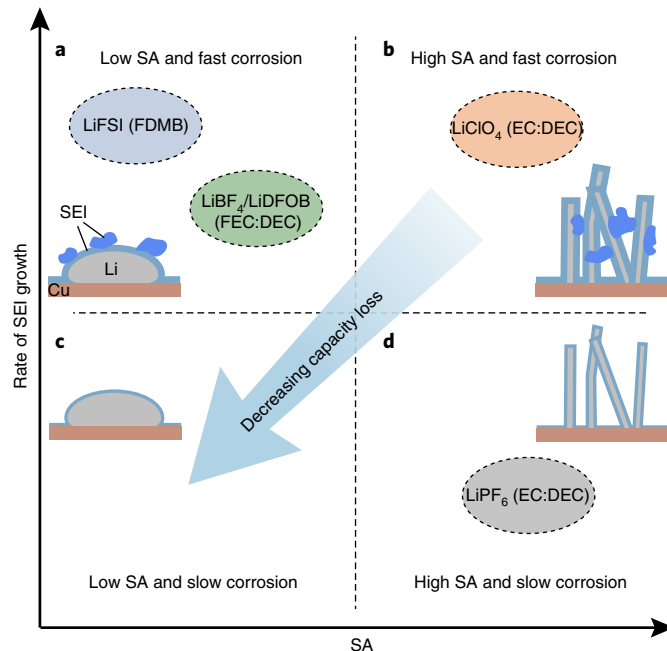


Fig. 5 | Schematic of the relationship between the rate of SEI growth, surface area (SA) of Li and capacity loss of Li metal anodes in liquid electrolytes. For clarity, the figure is separated into four sections of electrolyte chemistries. **a**, Electrolytes with fast corrosion of Li and low surface areas of Li. **b**, Electrolytes with fast corrosion of Li and high surface areas of Li. **c**, Electrolytes with slow corrosion of Li and low surface areas of Li. **d**, Electrolytes with slow corrosion of Li and high surface areas of Li. Capacity losses during calendar ageing of Li metal depend on developing an electrolyte that results in both the low surface area of Li and slow rate of SEI growth, or chemical corrosion.

demonstrates that electrolytes with thick or chunky microstructures of Li and high CE may not necessarily form strongly passivating SEI. Functional electrolytes must simultaneously optimize the microstructure of Li and minimize the rate of SEI growth.

Full-cell performance with ageing

The ΔCE value measures the impact of calendar ageing on a single cycle, but it is especially important to quantify the cumulative effect of ΔCE on the cycle life of LMBs. Figure 4 shows that calendar ageing shortens the cycle life of anode-free full-cells with $\text{LiBF}_4/\text{LiDFOB}$ (FEC:DEC) electrolyte and a LiFePO_4 (LFP) cathode. We use this cell chemistry as a representative example, because the electrolyte has strong performance in anode-free cells¹¹, and the stable working potential and long cycle life and calendar life of LFP²⁰ ensure that Li metal dominates the capacity losses.

The full-cell measurements are consistent with the $\text{Li}||\text{Cu}$ half-cell measurements in Fig. 1 and Supplementary Fig. 2. Without calendar ageing, the full-cells have a stable CE of 94.6% (Fig. 4a). They retain about 60% of their initial capacity after 12 cycles (Fig. 4b). The batteries aged for 24 hours in the charged state during every third cycle had a ΔCE of -2 to -4.5% in those same cycles (Fig. 4a). The consistency of the $\text{Li}||\text{Cu}$ and full-cell measurements suggests that the counter electrodes used in this study (that is, LFP or bulk Li) are not influencing ΔCE on these timescales. Although the CE increases slightly in the next cycle (likely caused by reactivation of electrochemically reversible SEI⁵² or dead Li⁵³), the average CE is 93.6%, a 1% decrease. The capacities of the batteries show equivalent results (Fig. 4b). Before any calendar ageing, there is no statistical difference between the batteries; however, after ageing, those batteries retain 60% of their initial capacity after only nine

cycles, a 25% decrease in cycle life (Fig. 4b). A higher frequency of ageing steps results in a shorter cycle life. Full-cells aged during every second and fifth cycle have 2.6% and 0.3% lower average CE, respectively, than cells without ageing (Supplementary Fig. 20). This extra few percent per cycle may seem inconsequential, but LIB can take about 500 days of calendar ageing to lose a similar amount of capacity⁵⁴. Improving the cycle life of Li metal remains critical, and as the cycle life improves, calendar ageing will become more important to consider with a variety of cathode chemistries.

The voltage profiles of the full-cells reinforce the expectation from the half-cell data in Figs. 1–3: SEI growth on Li causes the extra capacity loss after calendar ageing. Cells cycled without ageing have a gradual increase of hysteresis (Fig. 4c), which is caused by the steady build-up of SEI, dead Li and impedance during each cycle⁴. Voltage profiles of the full-cells aged during every third cycle show sharp increases of hysteresis in the cycles immediately after calendar ageing (Fig. 4d). $\text{Li}||\text{Cu}$ cells aged for 24 hours also have larger hysteresis after ageing (Supplementary Fig. 21). The extra growth of SEI during calendar ageing likely builds up impedance, causes larger hysteresis, and accelerates the loss of capacity.

Overall, future strategies to improve LMBs should consider the loss of Li during calendar ageing and its relation to the surface area of Li and rate of SEI growth (Fig. 5). The above data demonstrate that the electrolyte strongly affects these parameters. For example, LiClO_4 (EC:DEC) forms high surface areas of Li with fast chemical corrosion (Fig. 5b); LiPF_6 (EC:DEC) forms high surface areas of Li with slow chemical corrosion (Fig. 5d); and LiFSI (FDMB) and $\text{LiBF}_4/\text{LiDFOB}$ (FEC:DEC) form low surface areas of Li with fast corrosion (Fig. 5a). Further discovery of high-performance electrolyte chemistries is likely the most direct approach to optimize both parameters and approach Fig. 5c. Development of physical models for how the electrolyte chemistry affects the morphology and rate of SEI growth would accelerate this strategy. Combined approaches that use alloy-type current collectors to minimize surface area and strongly passivating electrolytes or protective films to prevent chemical corrosion could also minimize ΔCE .

Conclusions

This work quantifies the impact of calendar ageing on the rechargeability of Li metal anodes in a variety of electrolytes. Li metal typically loses about 2–3% of its capacity during 24 hours of calendar ageing for both high- and low-CE electrolytes. Direct visualization of the Li–SEI interface shows that the continuous growth of the SEI via chemical corrosion causes these losses of capacity. This growth of the SEI during calendar ageing is general, despite common thought that Li is resistant to corrosion in high-CE electrolytes. Each electrolyte forms a unique SEI chemistry, but two general types of SEI structure are observed. One is a compact, film-like and inorganic SEI that forms prior to calendar ageing, and the other is an extended, irregular and organic SEI that forms after calendar ageing. The magnitude of the capacity loss is related to the rate of SEI growth and surface area of Li in each electrolyte. High-CE electrolytes effectively minimize the surface area of Li, but they do not necessarily minimize the rate of SEI growth. Future electrolytes must simultaneously minimize corrosion and surface area. Furthermore, efforts should focus on reusing existing SEIs from previous cycles to minimize the impact of calendar ageing on the cycle life of Li metal batteries.

Methods

Materials preparation. All electrolytes were prepared and handled in an argon-filled glovebox with a O_2 concentration of $<0.2\text{ ppm}$ and H_2O concentration of $<0.01\text{ ppm}$. The 1 M LiPF_6 in EC:DEC electrolyte was used as received from Gotion LP 40. LiClO_4 (EC:DEC) was prepared with a 1:1 v/v mixture of EC (99+, Acros) and DEC (>99% anhydrous, Aldrich) with 1 M LiClO_4 (99% anhydrous, Acros Organics). LiFSI (1,2-dimethoxyethane (DME)) was prepared with 4 M LiFSI (Oakwood) and DME (Aldrich). LiTFSI (1,3-dioxolane (DOL):DME) with LiNO_3 was prepared with LiTFSI (Solvay), a 1:1 mixture of DME and DOL (Aldrich)

and 2.5% by weight LiNO₃ (Aldrich). The FDMB was synthesized by one-step methylation as described previously²⁷: to a 1 l round-bottom flask were added 300 ml dry tetrahydrofuran (THF) and 64 g 2,2,3,3-tetrafluoro-1,4-butanediol. The solution was cooled to 0 °C, and then 40 g NaH were added slowly. Bubbling was observed upon NaH addition. Then, 100 g MeI were added dropwise to the stirring suspension. The suspension was allowed to warm up to room temperature and then refluxed overnight at 60 °C. The mixture was then filtered off and the solvents were removed under vacuum. The crude product was vacuum distilled to yield the final product as a colourless liquid. The product was then filtered off through a 0.45 µm polytetrafluoroethylene (PTFE) filter and moved to an argon glovebox for further use. The yield was ~85%.

The NMR specifications were as follows: ¹H NMR (THF-d8, 400 MHz): δ 3.85–3.76 ppm (*m*, 4H), 3.42 ppm (*s*, 6H). ¹³C NMR (THF-d8, 100 MHz): δ 119.09–114.06 ppm, 69.54–69.02 ppm, 59.48 ppm. ¹⁹F NMR (THF-d8, 376 MHz): δ –123.50 ppm (*m*, 4F).

The wrinkly graphene was prepared as described previously²⁸: 2 g of spiky nickel powder (Novamet) dispersed in 150 ml of deionized water was added to 1 ml of 1 M trisodium citrate (Sigma). Next, 2 ml of 6.75 mM HAuCl₄ (Sigma) was added under vigorous stirring. The reaction was held at room temperature for 10 min, and spiky nickel powder was then filtered and dried in a vacuum oven for 4 h. After drying, the powder was dispersed in 200 ml of triethylene glycol (Sigma) and stirred overnight at 250 °C. The resulting suspension was centrifuged and washed with ethanol five times and dried in a vacuum oven overnight. The dried powder was placed in a tube furnace with an Ar flow rate of 80 sccm and a temperature profile of heating to 100 °C at 2 °C min⁻¹; heating to 450 °C at 20 °C min⁻¹; and holding at 450 °C for 1 h. The resulting graphene-covered nickel powder was etched in 1 M:1 M FeCl₃/HCl solution overnight and then filtered, washed and dried in a vacuum oven.

The wrinkly graphene powder was then cast onto Cu foil using a conventional slurry and doctor-blading technique. The slurry consisted of wrinkly graphene powder and polyvinylidene fluoride (Kynar HSV 900) binder with a mass ratio of 9:1 dispersed in *N*-methyl-2-pyrrolidone. The slurry was stirred for 12 h, then cast onto a Cu foil and dried at 60 °C in a vacuum oven for 6 h. Electrodes were then punched into 1 cm² discs.

Electrochemical methods. Unless specified otherwise, electrochemical measurements used 2032-type coin-cells with 60 µl of electrolyte. High-purity Li foil (750 µm, 99.9% (Alfa Aesar)) and Cu foil (Pred Materials) were used in all experiments. Both the Li and Cu foils were punched to 1 cm². Cu was rinsed with deionized water, ethanol (Fisher) and acetone (Fisher) prior to transferring to the Ar glovebox for coin-cell assembly to remove surface contaminants. Lithium was mechanically sheared with a polyethylene scraper to remove the surface oxide and improve electrical connection to the stainless-steel coin-cell. Once the coin-cell was fabricated, we formed an SEI on the Cu substrate by holding the Li || Cu cell at 0 V for 24 hours prior to cycling and used the CE of the second cycle as the measurable quantity. This protocol minimized errors from incomplete passivation of the Cu and more closely simulated situations where the SEI is stabilized. CE data were collected on an Arbin battery cycler at 25 °C unless specified otherwise.

Li || Li symmetric cells were prepared in an argon-filled glovebox with 60 µl of electrolyte in a coin-cell configuration. Two 1 cm² lithium electrodes were polished and pressed onto stainless-steel spacers to ensure the electrodes were flat. Some 2032-type coin-cells were used with 25-micrometre-thick polypropylene-polyethylene-polypropylene separators (Celgard). The first EIS measurement was made immediately after cell assembly, and approximately 5 minutes after the initial contact of the electrolyte with lithium. The measurements were made at open circuit, and a frequency range of 1 MHz to 0.2 Hz was used with a perturbation amplitude of 5 mV. The impedance of Li was continuously measured for three days.

The raw data were averaged between the two equivalent Li electrodes (that is, dividing by two) and normalized to the surface area of one lithium electrode (1 cm²). The time-dependent interfacial resistance ($R_{int}(t)$) was calculated by fitting the Nyquist plot of the EIS measurement to a well-accepted equivalent circuit for lithium anodes, which is a series of resistor/capacitor (R/C) circuits, using the equivalent circuit fitting feature of Biologic's EC-Lab software^{46,55}. The sum of the resistances in the equivalent circuit give the total interfacial resistance (R_{int}), which corresponds to the total width of the semicircle in the Nyquist plots. The R_{int} value was calculated for times of 0.25, 1, 5, 10, 24, 48 and 72 hours. Representative Nyquist plots for each electrolyte chemistry are shown in Supplementary Fig. 19, and calculated parameters are reported below.

The $R_{int}(t)$ was fit to an empirical power law (that is $R_{int}(t) = At^{\alpha}$), which is typically used to describe SEI growth⁴⁴, via non-linear least squares fitting. The Python package optimize.curvefit was used, and the calculated parameters and calculated variances of the parameters are reported in Supplementary Table 2.

Soem 2032-type coin-cells with a 1 cm² Cu foil anode (Pred Materials), 1 cm² LFP (2 mA h cm⁻² loading, MTI) and 60 µl of LiBF₄/LiDFOB in FEC:DEC were used for cycling. The Cu was prepared and rinsed using the same procedure as those in the half-cell measurements. Once the coin-cell was fabricated, two slow formation cycles (C/10, 0.2 mA cm⁻²) were run, after which the cell was cycled at a moderate rate (C/2, 1 mA cm⁻²), where C is the charging rate required to fully charge the battery in 1 hour, and C/10 denotes one tenth of the C-rate. Cut-off voltages were 3 V for discharge and 4 V for charge. Standard cycling included no calendar ageing.

For the cells with ageing intervals, the cells were aged at 100% state of charge for 24 hours during every third or fifth cycle.

Materials characterization. The batteries for cryo-TEM analysis were disassembled in an argon-filled glovebox and rinsed with DEC to remove Li salts. Our rinsing procedure attempts to minimize artefacts by using minimal force and solvent volume; approximately 20 µl was carefully dropped onto the TEM grid after the battery was disassembled. Immediately after rinsing, the sample was sealed in an air-tight container and submerged in liquid nitrogen, and the container was crushed to rapidly expose the sample to cryogen without any air exposure. While immersed in liquid nitrogen, the sample was loaded into the cryo-TEM holder (Gatan 626) and inserted into the TEM column. The cryo-TEM holder uses a specialized shutter to prevent air exposure and condensation onto the sample, which preserves the specimen in its native state. Once inside the TEM column, the sample temperature was maintained at approximately –176 °C.

All cryo-(S)TEM characterizations were carried out using an FEI Titan 80–300 environmental (scanning) transmission electron microscope operated at an accelerating voltage of 300 kV. Cryo-STEM EELS characterization was performed with a C2 aperture of 50 µm, a beam current of 75 pA, a camera length of 48 mm and a pixel dwell time of 10 ms. These settings give a convergence angle of 9.3 mrad and an acceptor angle of 27.8 mrad. EELS spectra were acquired on a Gif Quantum 966 with a dispersion of 0.25 or 0.5 eV per channel in Dual EELS mode. The energy resolution was approximately 1.25–2 eV, measured through the full width half maximum of the zero-loss peak. Energy drift during spectrum imaging was corrected by centring the zero-loss peak to 0 eV at each pixel. The EELS fine structures used electron dosages of 70–150 e Å^{–2}, which is well below the dosage where carbonaceous SEI components are unstable (10⁴ e Å^{–2}). Maps were computed through a two-window method, with a pre-edge window fitted to a power-law background and a post-edge window of 20–40 eV on the core-loss signal. TEM imaging was performed using a K3 IS camera (Gatan). XPS characterization was performed on a PHI Versaprobe I with a monochromatized Al Kα X-ray source. The chamber was kept at a pressure of about 10^{–7} Pa during characterization. High-purity Li foil (750 µm, 99.9%, Alfa Aesar) was used. The unrested Li was exposed to electrolyte for only about 2–5 minutes. Rested cells were aged in the electrolyte for 24 hours. Prior to characterization, the surface was rinsed with 60 µl of pure DEC (>99% anhydrous, Aldrich) in an Ar-filled glovebox to remove residual salt. A vacuum transfer vessel was used to transfer the samples directly from the Ar glovebox to the vacuum transfer chamber of the instrument to prevent air exposure. Gentle sputtering conditions (1 kV, 0.5 µA, 1 mm × 1 mm) were used for the first two sputtering cycles followed by 2 kV, 1 µA and 1 mm × 1 mm for the next two sputtering cycles in the rested case. The sputtering depths correspond to 0, 4, 8, 23 and 38 nm of SiO₂.

Data availability

The datasets analysed and generated during the current study are included in the paper and its Supplementary Information file.

Received: 4 August 2020; Accepted: 29 January 2021;

Published online: 22 March 2021

References

- Xu, W. et al. Lithium metal anodes for rechargeable batteries. *Energy Environ. Sci.* **7**, 513–537 (2014).
- Lin, D., Liu, Y. & Cui, Y. Reviving the lithium metal anode for high-energy batteries. *Nat. Nanotechnol.* **12**, 194–206 (2017).
- Fang, C., Wang, X. & Meng, Y. S. Key issues hindering a practical lithium-metal anode. *Trends Chem.* **1**, 152–158 (2019).
- Fang, C. et al. Quantifying inactive lithium in lithium metal batteries. *Nature* **572**, 511–515 (2019).
- Zachman, M. J., Tu, Z., Choudhury, S., Archer, L. A. & Kourkoutis, L. F. Cryo-STEM mapping of solid–liquid interfaces and dendrites in lithium–metal batteries. *Nature* **560**, 345–349 (2018).
- Li, Y. et al. Correlating structure and function of battery interphases at atomic resolution using cryoelectron microscopy. *Joule* **2**, 2167–2177 (2018).
- Li, Y. et al. Atomic structure of sensitive battery materials and interfaces revealed by cryo-electron microscopy. *Science* **358**, 506–510 (2017).
- Wang, X. et al. New insights on the structure of electrochemically deposited lithium metal and its solid electrolyte interphases via cryogenic TEM. *Nano Lett.* **17**, 7606–7612 (2017).
- Lin, D. et al. Layered reduced graphene oxide with nanoscale interlayer gaps as a stable host for lithium metal anodes. *Nat. Nanotechnol.* **11**, 626–632 (2016).
- Cao, X. et al. Monolithic solid–electrolyte interphases formed in fluorinated orthoformate-based electrolytes minimize Li depletion and pulverization. *Nat. Energy* **4**, 796–805 (2019).
- Weber, R. et al. Long cycle life and dendrite-free lithium morphology in anode-free lithium pouch cells enabled by a dual-salt liquid electrolyte. *Nat. Energy* **4**, 683–689 (2019).
- Niu, C. et al. Self-smoothing anode for achieving high-energy lithium metal batteries under realistic conditions. *Nat. Nanotechnol.* **14**, 594–601 (2019).

13. Gao, Y. et al. Polymer-inorganic solid-electrolyte interphase for stable lithium metal batteries under lean electrolyte conditions. *Nat. Mater.* **18**, 384–389 (2019).
14. Adams, B. D., Zheng, J., Ren, X., Xu, W. & Zhang, J. G. Accurate determination of Coulombic efficiency for lithium metal anodes and lithium metal batteries. *Adv. Energy Mater.* **8**, 1702097 (2017).
15. Crozier, C., Apostolopoulou, D. & McCulloch, M. Clustering of usage profiles for electric vehicle behaviour analysis. In *2018 IEEE PES Innovative Smart Grid Technologies Conference Europe (ISGT-Europe)* 1–6 (IEEE, 2018).
16. Speidel, S. & Bräunl, T. Driving and charging patterns of electric vehicles for energy usage. *Renew. Sustain. Energy Rev.* **40**, 97–110 (2014).
17. Kolesnikov, A. et al. Galvanic corrosion of lithium-powder-based electrodes. *Adv. Energy Mater.* **10**, 2000017 (2020).
18. Lin, D. et al. Fast galvanic lithium corrosion involving a Kirkendall-type mechanism. *Nat. Chem.* **11**, 382–389 (2019).
19. Keil, P. et al. Calendar aging of lithium-ion batteries I. Impact of the graphite anode on capacity fade. *J. Electrochem. Soc.* **163**, A1872–A1880 (2016).
20. Dubarry, M., Qin, N. & Brooker, P. Calendar aging of commercial Li-ion cells of different chemistries – a review. *Curr. Opin. Electrochem.* **9**, 106–113 (2018).
21. Attia, P. M., Das, S., Harris, S. J., Bazant, M. Z. & Chueh, W. C. Electrochemical kinetics of SEI growth on carbon black: part I. Experiments. *J. Electrochem. Soc.* **166**, 97–106 (2019).
22. Moretti, A. et al. A comparison of formation methods for graphite//LiFePO₄ cells. *Batter. Supercaps* **2**, 240–247 (2019).
23. Qian, J. et al. High rate and stable cycling of lithium metal anode. *Nat. Commun.* **6**, 6362 (2015).
24. Yu, Z. et al. Molecular design of electrolyte solvents enabling energy-dense and long-cycling lithium metal batteries. *Nat. Energy* **5**, 526–533 (2020).
25. Liu, Y. et al. Solubility-mediated sustained release enabling nitrate additive in carbonate electrolytes for stable lithium metal anode. *Nat. Commun.* **9**, 3656 (2018).
26. Peled, E. & Menkin, S. Review—SEI: past, present and future. *J. Electrochem. Soc.* **164**, A1703–A1719 (2017).
27. Genovese, M. et al. Hot formation for improved low temperature cycling of anode-free lithium metal batteries. *J. Electrochem. Soc.* **166**, A3342–A3347 (2019).
28. Wang, J. et al. Improving cyclability of Li metal batteries at elevated temperatures and its origin revealed by cryo-electron microscopy. *Nat. Energy* **4**, 664–670 (2019).
29. Wang, H. et al. Wrinkled graphene cages as hosts for high-capacity Li metal anodes shown by cryogenic electron microscopy. *Nano Lett.* **19**, 1326–1335 (2019).
30. Pei, A., Zheng, G., Shi, F., Li, Y. & Cui, Y. Nanoscale nucleation and growth of electrodeposited lithium metal. *Nano Lett.* **17**, 1132–1139 (2017).
31. Huang, W. et al. Evolution of the solid-electrolyte interphase on carbonaceous anodes visualized by atomic-resolution cryogenic electron microscopy. *Nano Lett.* **19**, 5140–5148 (2019).
32. Huang, W. et al. Dynamic structure and chemistry of the silicon solid-electrolyte interphase visualized by cryogenic electron microscopy. *Mater.* **1**, 1232–1245 (2019).
33. Pinson, M. B. & Bazant, M. Z. Theory of SEI formation in rechargeable batteries: capacity fade, accelerated aging and lifetime prediction. *J. Electrochem. Soc.* **160**, A243–A250 (2013).
34. Zhou, Y. et al. Real-time mass spectrometric characterization of the solid-electrolyte interphase of a lithium-ion battery. *Nat. Nanotechnol.* **15**, 224–230 (2020).
35. Lu, P., Li, C., Schneider, E. W. & Harris, S. J. Chemistry, impedance, and morphology evolution in solid electrolyte interphase films during formation in lithium ion batteries. *J. Phys. Chem. C* **118**, 896–903 (2014).
36. Huang, W., Wang, H., Boyle, D. T., Li, Y. & Cui, Y. Resolving nanoscopic and mesoscopic heterogeneity of fluorinated species in battery solid-electrolyte interphases by cryogenic electron microscopy. *ACS Energy Lett.* **5**, 1128–1135 (2020).
37. Xu, K. Nonaqueous liquid electrolytes for lithium-based rechargeable batteries. *Chem. Rev.* **104**, 4303–4417 (2004).
38. Brown, Z. L., Jurng, S., Nguyen, C. C. & Lucht, B. L. Effect of fluoroethylene carbonate electrolytes on the nanostructure of the solid electrolyte interphase and performance of lithium metal anodes. *ACS Appl. Energy Mater.* **1**, 26–31 (2018).
39. Cody, G. D. et al. Quantitative organic and light-element analysis of comet 81P/Wild 2 particles using C-, N-, and O- μ -XANES. *Meteorit. Planet. Sci.* **43**, 353–365 (2008).
40. le Guillou, C., Bernard, S., de la Pena, F. & le Brech, Y. XANES-based quantification of carbon functional group concentrations. *Anal. Chem.* **90**, 8379–8386 (2018).
41. Braun, A., Kubatova, A., Wirick, S. & Mun, S. B. Radiation damage from EELS and NEXAFS in diesel soot and diesel soot extracts. *J. Electron Spectrosc. Relat. Phenom.* **170**, 42–48 (2009).
42. Endo, E., Ata, M., Sekai, K. & Tanaka, K. Spin trapping study of gradual decomposition of electrolyte solutions for lithium secondary batteries. *J. Electrochem. Soc.* **146**, 49–53 (1999).
43. Gourdin, G., Collins, J., Zheng, D., Foster, M. & Qu, D. Spectroscopic compositional analysis of electrolyte during initial SEI layer formation. *J. Phys. Chem. C* **118**, 17383–17394 (2014).
44. Soto, F. A. et al. Formation and growth mechanisms of solid-electrolyte interphase layers in rechargeable batteries. *Chem. Mater.* **27**, 7990–8000 (2015).
45. Huang, W. et al. Nanostructural and electrochemical evolution of the solid-electrolyte interphase on CuO nanowires revealed by cryogenic electron microscopy and impedance spectroscopy. *ACS Nano* **13**, 737–744 (2019).
46. Boyle, D. T. et al. Transient voltammetry with ultramicroelectrodes reveals the electron transfer kinetics of lithium metal anodes. *ACS Energy Lett.* **5**, 701–709 (2020).
47. Wood, S. M. et al. Predicting calendar aging in lithium metal secondary batteries: the impacts of solid electrolyte interphase composition and stability. *Adv. Energy Mater.* **8**, 1801427 (2018).
48. Attia, P. M., Cheuh, W. C. & Harris, S. J. Revisiting the $t^{0.5}$ dependence of SEI growth. *J. Electrochem. Soc.* **167**, 090535 (2020).
49. Aurbach, D. & Zaban, J. Impedance spectroscopy of lithium electrodes: part 1. General behavior in propylene carbonate solutions and the correlation to surface chemistry and cycling efficiency. *J. Electroanal. Chem.* **348**, 155–179 (1993).
50. Aurbach, D. & Zaban, J. Impedance spectroscopy of lithium electrodes: part 2. The behaviour in propylene carbonate solutions — the significance of the data obtained. *J. Electroanal. Chem.* **367**, 15–25 (1994).
51. Aurbach, D. & Zaban, J. Impedance spectroscopy of lithium electrodes: part 3. The importance of Li electrode preparation. *J. Electroanal. Chem.* **365**, 41–45 (1994).
52. Zhuo, Z. et al. Breathing and oscillating growth of solid-electrolyte-interphase upon electrochemical cycling. *Chem. Commun.* **54**, 814–817 (2018).
53. Zheng, J. et al. Physical orphaning versus chemical Instability: is dendritic electrodeposition of Li fatal? *ACS Energy Lett.* **4**, 1349–1355 (2019).
54. Harlow, J. E. et al. A wide range of testing on an excellent lithium-ion cell chemistry to be used as benchmarks for new battery technologies. *J. Electrochem. Soc.* **166**, A3031–A3044 (2019).
55. Zaban, A., Zinigrad, E. & Aurbach, D. Impedance spectroscopy of lithium electrodes. 4. A general simple model of the Li-solution interphase in polar aprotic systems. *J. Phys. Chem.* **100**, 3089–3101 (1996).

Acknowledgements

We acknowledge support from the Assistant Secretary for Energy Efficiency and Renewable Energy, Office of Vehicle Technologies of the US Department of Energy under the Battery Materials Research (BMR) Program and Battery 500 Consortium. The cryo-TEM research is supported by the Department of Energy, Office of Basic Energy Sciences, Division of Materials Science and Engineering under contract DE-AC02-76SF00515. D.T.B. acknowledges support from the National Science Foundation Graduate Research Fellowship Program. Scanning electron microscopy and TEM were performed at the Stanford Nano Shared Facilities (SNSF), supported by the National Science Foundation under award ECCS-1542152. The K3 IS camera and support are courtesy of Gatan. We also acknowledge H. Wang for help designing the schematic in Fig. 5.

Author contributions

D.T.B. and Y.C. conceived the idea. D.T.B. designed the research with guidance from Y.C., carried out the electrochemical measurements and analysed the data. W.H. and Y.L. helped design the cryo-(S)TEM experiments, and W.H. carried out the cryo-(S)TEM experiments and analysed the data. W.Z. carried out the cryo-TEM selected area electron diffraction (SAED) and additional EELS measurements. H.W. and H.C. helped carry out and interpret the XPS experiments and synthesized host materials. H.C. helped with scanning electron microscopy. Z.Y. synthesized electrolyte materials. D.T.B., W.H. and Y.C. wrote the manuscript.

Competing interests

The authors declare no competing interests.

Additional information

Supplementary information The online version contains supplementary material available at <https://doi.org/10.1038/s41560-021-00787-9>.

Correspondence and requests for materials should be addressed to Y.C.

Peer review information *Nature Energy* thanks Marian Stan, Yifei Yuan and the other, anonymous, reviewer(s) for their contribution to the peer review of this work.

Reprints and permissions information is available at www.nature.com/reprints.

Publisher's note Springer Nature remains neutral with regard to jurisdictional claims in published maps and institutional affiliations.

© The Author(s), under exclusive licence to Springer Nature Limited 2021